Sub-GHz Resolution Photonic Spectral Processor and Its System Applications

Roy Rudnick, Alexander Tolmachev, David Sinefeld, Ori Golani, Shalva Ben-Ezra,
Moshe Nazarathy, *Senior Member, IEEE, Fellow, OSA*, and Dan M. Marom, *Senior Member, IEEE, Fellow, OSA*

***Abstract*—A record performance metric waveguide grating router (WGR) design with a 200 GHz free spectral range (FSR) capable of resolving sub-GHz resolution spectral features is developed for a fine resolution photonic spectral processor (PSP). The WGR's FSR was designed to support subchannel add/drop from a superchannel of 1 Tb/s capacity. Due to fabrication imperfections, we introduce phase corrections to the light beams emerging from the 250 waveguides of the WGR output using a liquid crystal on silicon (LCoS) phase spatial light modulator (SLM) placed in an imaging configuration. A second LCoS SLM is located at the Fourier plane, for arbitrary spectral amplitude and phase manipulations. The PSP is utilized in multiple system transmission experiments, such as flexible spectral shaping and subcarrier drop demultiplexing with sub-GHz spectral resolution.**

***Index Terms*—Optical communication, optical filters, optical planar waveguide components, optical waveguide components, wavelength division multiplexing.**

I. Introduction

LINEAR optical signal processing operations can assist optical communications in performing myriads of operations such as wavelength multiplexing, wavelength selective switching (WSS), and complex spectral filtering for channel selection, dispersion compensation, and signal shaping. Adaptive filtering operations are of particular interest, enabling tuning of the center wavelength, selected bandwidth, dispersion compensation level and signal format conversion. Performing these operations with a spatial light modulator (SLM) operating on spatially dispersed light has been demonstrated [1]–[3]. These and similar experiments are based on a WSS platform, using a dispersive free-space optics arrangement with a bulk diffraction grating and lenses (an optical arrangement originating from ultrashort pulse shaping [4], [5]), and replacing the channelized micro-mirror SLM [6] with a liquid crystal on silicon (LCoS) SLM for finer control [7]. The performance of these WSS based instruments is set by the spectral resolution of the dispersing arrangement (typically 5–10 GHz) and the pixel pitch determining spectral addressability (few GHz). Such spectral resolution and addressability is sufficient for DWDM channel selection, which is the target application of a WSS. However, these spectral specifications fall short of those required to optimally support intra-channel filtering requirements in telecom applications (e.g. Ref [2] tried unsuccessfully to optically shape a transmitted signal with a WSS-based instrument, whereas in [8] a specialized filter extended the reach of a duobinary signal). Improved optical resolution metrics can be obtained by replacing the bulk diffraction grating dispersive element with a waveguide grating router (WGR) [9], [10] or a virtually imaged phased array (VIPA) [11], [12], both of which can be designed to provide larger dispersion values over a finite free spectral range (FSR). These larger dispersion devices provide finer optical resolution for intra-channel spectral filtering, giving the filtering apparatus the moniker *photonic spectral processor* (PSP). Our PSP is based on a hybrid guided wave and free-space optics arrangement, where the WGR, implemented in silica waveguides, angularly disperses the light. The diffracted light is then focused by a Fourier lens onto an LCoS, two-dimensional phase SLM. With the LCoS SLM we are able to prescribe phase and amplitude onto the signal's spatially dispersed spectral components. In this Paper, we vastly improve the fine-resolution filtering attributes of a WGR-based PSP.

Our new PSP implementation is based on a WGR designed to obtain 0.8 GHz optical resolution over a 200 GHz FSR (Fig. 1). Similar resolution was demonstrated before for a WGR demultiplexer (demux) over a 16 GHz FSR [13]. Obtaining such resolution attributes requires very large delays within the WGR, while still maintaining phase accuracy at the output. Unfortunately, these requirements are beyond standard fabrication tolerances, resulting in the WGR having excessive phase errors which completely destroys the constructive phased array interference at the output. In [13], individual waveguides were phase trimmed with ultra-violet (UV) irradiation after hydrogen loading. We employed a phase compensation technique based on a phase SLM to correct the individual waveguide's phase errors and obtain the true optical resolution of the fabricated WGR, similar to that first reported in [14] where we used a 50 GHz FSR

Manuscript received September 18, 2016; revised December 7, 2016; accepted December 24, 2016. Date of publication January 3, 2017; date of current version April 20, 2017. This work was supported in part by the EC FP7-ICT Project FOX-C under Grant 318415, in part by ASTRON under Grant 318714, and in part by the Israel Ministry of Economics, Tera-Santa Program.

R. Rudnick, D. Sinefeld, O. Golani, and D. M. Marom are with the Applied Physics Department, Hebrew University of Jerusalem, Jerusalem 9190501, Israel (e-mail: roi.rudnick@gmail.com; sinefeld@gmail.com; ori.golani@mail.huji.ac.il; danmarom@mail.huji.ac.il).

A. Tolmachev and M. Nazarathy are with the Electrical Engineering Department, Technion, Haifa 3200003, Israel (e-mail: talex@tx.technion.ac.il; nazarat@ee.technion.ac.il).

S. Ben-Ezra is with the Finisar-Israel, Holon 5885849, Israel (e-mail: shalva.ben-ezra@finisar.com).

Color versions of one or more of the figures in this paper are available online at http://ieeexplore.ieee.org.

Digital Object Identifier 10.1109/JLT.2016.2647710

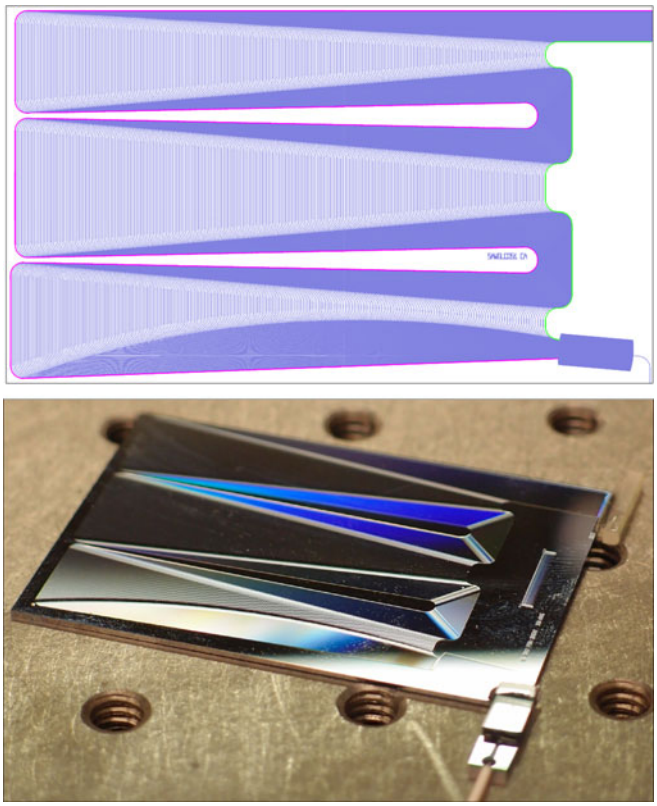

Fig. 1. Waveguide grating router with sub-GHz optical resolution. Top: Design layout with 250 waveguides (dimensions ~4 × 5 cm). Longest waveguide colored magenta, shortest in green, for better visualization. Bottom: WGR with I/O fiber attached and cylindrical lens to collimate output radiating light in the guided (vertical) direction.

WGR consisting of 63 waveguides. In that previous work [14] we did not obtain the WGR's designed resolution, yet were able to achieve 1 GHz resolution metric. We have since improved our correction scheme, and performed it over 250 waveguides covering a 200 GHz FSR, as first reported in [15], and provide the full technical details in this paper.

The record performance metrics of the PSP allow synthesizing complex spectral filtering functions with extremely sharp features nearly matching ideal characteristics. We demonstrate our fine resolution PSP in telecom applications, demonstrating the utility of fine resolution adaptive optical filters in novel joint photonic-digital receiver (Rx) signal processing applications.

II. Fine Resolution Waveguide Grating Router Design

WGRs were originally developed for optical demultiplexing functionality in wavelength division multiplexing (WDM) systems [16]–[18]. A WGR demux employs a first star coupler (free space region) allowing an input waveguide to radiate into the waveguide array, followed by a second star coupler where the dispersed light emerging from the waveguide array is coupled to individual demultiplexed output waveguides. Such demux WGRs are attractive in that they are compact, easily packaged and robust, due to guiding in high refractive index contrast waveguides allowing sharp bends on a planar lightwave circuit (PLC). The dispersive medium we utilize for our PSP application is an unconventional WGR, where we discard the second slab lens region that demultiplexes to output waveguides. The grating arms terminate at the PLC edge, allowing the light to radiate into free space. This forms a phased-array output that experiences angular dispersion on account of wavelength-dependent phase delays in the waveguide array. Using an external Fourier lens, we obtain spatially dispersed light allowing for manipulation in free space with an SLM.

The key design features of a WGR are its incremental path length increase, ΔL, between successive waveguides and number of waveguides, N, within the array. The former sets the FSR according to $\nu_{\mathrm{FSR}} = c/(n_g \cdot \Delta L)$ (where n_g is the group index of the waveguide propagating mode and c is the speed of light) and the latter sets the spectral resolution $\nu_{\mathrm{res}} \cong \nu_{\mathrm{FSR}}/N$. The WGR was designed with 200 GHz FSR and 250 waveguide arms to support spectral super-channels of 1 Tb/s capacity [19]. The WGR was implemented in a silica on silicon platform with 2% index contrast waveguides of 4×4 μm cross-section (Fig. 1-bottom) with $n_{\mathrm{eff}} \cong 1.46$ (n_{eff} is the effective index of the waveguide propagating mode at the design wavelength). The WGR's $N = 250$ waveguide arms have a relative path length difference of $\Delta L = m \cdot \lambda_0/n_{\mathrm{eff}} = \sim 1$ mm (where $m = 935$ is the diffraction order), for a total WGR path length difference of $N \cdot \Delta L = 250$ mm. The inverse of the time delay ($\Delta t = N \cdot \Delta L/\nu_{\mathrm{g}} = 1.25$ ns) matches our 0.8 GHz target resolution, in line with time-bandwidth uncertainty principle. To obtain a compact WGR design for such a long path difference, the waveguides are folded three times within the PLC (total size is 5×4 cm) (Fig. 1-top). Light from an input waveguide excites the 250 waveguide arms via a confocal slab lens of ~8 mm radius. Power distribution across the waveguides was Gaussian, with edge waveguides having approximately 10 dB lower power than central waveguides. The waveguides taper out at the slab lens to efficiently collect 75% of the input power. Following the slab lens, the waveguide arms are routed with differential lengths to the edge of the PLC (Fig. 1). Waveguide spacing within the WGR was chosen so that coupling between adjacent routes is negligible. The pitch p at the output (at the PLC edge) is 18.6 μm, and the waveguides are adiabatically broadened to size $\Delta_{\mathrm{wg}} = 17$ μm. The optical field at the WGR's output facet is described by the contribution of each waveguide i in the array

$$E_{\mathrm{WGR}}(\xi,\nu) = \sum_i a_i \cdot \phi\left(\frac{\xi - i\cdot p}{\Delta_{\mathrm{wg}}}\right) \cdot \exp\left[j2\pi i m\left(1 + \frac{n_g}{n_{\mathrm{eff}}}\cdot\frac{\nu-\nu_0}{\nu_0}\right)\right] \quad (1)$$

where a_{i} is the Gaussian amplitude apodization, applied over all waveguides, which originates from WGR's star coupler (see dashed line in Fig. 2-top), $\phi(\bullet)$ represents a Gaussian mode of an individual waveguide located at $\xi = i \cdot p$, with an accumulated phase (argument of the exponent) that is dependent on the diffraction order, effective and group refractive indexes, and the optical temporal frequency. The phased array light output of the WGR at the PLC facet is Fourier transformed with lens f,

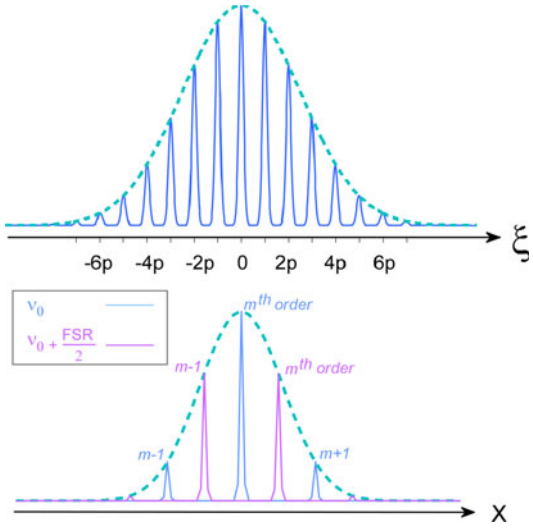

Fig. 2. Top: Depiction of Gaussian apodization of a WGR output with a waveguide pitch p. Bottom: The Fourier transform of WGR output, where the envelope is the Fourier transform of a single waveguide Gaussian mode. The diffraction orders exist underneath this curve. Blue: Diffraction orders at the designed ν_0 frequency. Purple: Diffraction orders at the $\nu_0 + \mathrm{FSR}/2$ frequency.

yielding:

$$E_{\mathrm{spec}}(x,\nu) = \phi\left(\frac{\Delta_{\mathrm{wg}}\cdot x}{\lambda_0\cdot f}\right) \cdot \sum_i \phi\left(\frac{x}{\Delta_{\mathrm{cw}}} - \frac{\lambda_0\cdot f}{\Delta_{\mathrm{cw}}\cdot p}\left(i+m+m\frac{n_g}{n_{\mathrm{eff}}}\cdot\frac{\nu-\nu_0}{\nu_0}\right)\right) \tag{2}$$

where the Gaussian mode, ϕ, of the individual WGR's waveguides of size Δ_{wg} determines the far field interference pattern envelope (the first term in Eq. (2), see dashed line in Fig. 2-bottom). The sum term is the constructive interference of the Gaussian apodized WGR output, with the -m'th diffraction order being of interest. Since the apodization is Gaussian, the constructive interference is too. Each spectral component creates multiple diffraction orders, each of size $\Delta_{\mathrm{cw}} \approx 4\cdot\lambda\cdot f/(\pi\cdot\Delta_{\mathrm{WGR}})$ where Δ_{WGR} is the WGR overall output mode size, their spacing being inversely proportional to the waveguide array pitch, p. The number of excited diffraction orders depends on the extent of the far field interference pattern envelope. Hence having narrow waveguides relative to the waveguide pitch would undesirably result in the excitation of many diffraction orders. To minimize the diffraction order excitation count, we adiabatically broaden the waveguides at the WGR output from 4 μm to $\Delta_{\mathrm{wg}} = 17\,\mu$m, on $p = 18.6\,\mu$m pitch.

From Eq. (2) we calculate the spatial dispersion by simple differentiation:

$$\frac{dx}{d\nu} = \frac{c\cdot m\cdot f}{\nu_0^2\cdot p}\cdot\frac{n_g}{n_{\mathrm{eff}}} \tag{3}$$

Our Fourier transform lens is of $f = 50$ mm, thus obtaining spatial dispersion of 20 μm/GHz. For efficient coupling to the input/output fiber, a mode converter section was used to match the mode shapes of the 4×4 μm waveguide and the single mode fiber. Fiber to PLC coupling loss of -0.5 dB was achieved. A total loss (one way) of $\sim$2 dB was observed. This additional loss derives mostly from the star coupler in the WGR design. The PLC facets were polished, and a 1.5 mm focal length high NA cylindrical lens was attached at the output facet to collimate the light in the guided (vertical) direction.

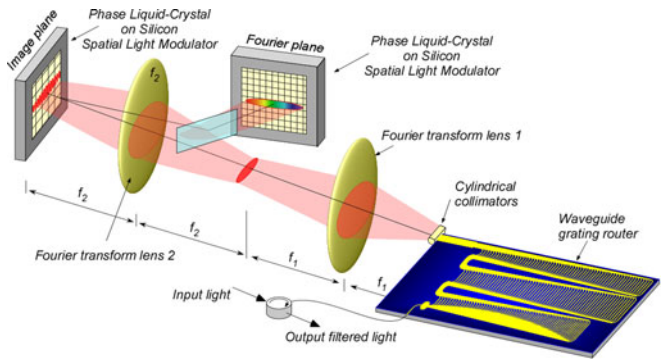

Fig. 3. Experimental setup for compensation of WGR phase errors with an LCoS phase modulator and spectral processing in the Fourier plane.

The far field radiation from the WGR should be spectrally resolved, as predicted by Eq. (2), and allow filtering by an SLM. In practice, we did not observe a spectrally resolved signal due to phase errors on each waveguide. Many factors may contribute to the sources of phase errors, such as lithography/etching errors, core thickness variations, refractive index inhomogeneity and/or stress.

III. Active Phase Error Compensation With an LCoS SLM

To circumvent the phase error problem, we devised an optical arrangement that first images the PLC output facet onto an LCoS SLM at a secondary plane with a magnification factor of $M = 3$ (labeled 'image plane' in Fig. 3). This magnification factor was chosen to map the WGR array output width ($18.6\,\mu\mathrm{m}\times250 = 4.65$ mm) to $\sim$14 mm, efficiently spanning the LCoS SLM width (Holoeye Pluto, 1920 $\times$ 1080 pixels at $8\,\mu$m/pixel $= 15.36\times8.64$ mm). The waveguide pitch of 18.6 μm is thus magnified to 55.8 μm, equaling 7 pixels on the SLM. Each waveguide output mode occupies a unique position on the SLM, and we can modulate the phase of the individual reflected light beams by applying a voltage onto the underlying pixels. The 7 pixel span also helps reduce the fringing field impact between adjacent LCoS pixels at different voltage setting. The reflected light from the image plane, consisting of the phase modulated waveguide array spots, is then Fourier transformed onto the spectrally resolved plane (labeled 'Fourier plane' in Fig. 3). If the phase of each output waveguide in the array is properly adjusted, then the constructive interference pattern of the waveguide array focuses to a tight spot (at the -m'th order) with adjacent diffraction orders present (per Eq. (2), when excited by single frequency light). Different wavelengths accumulate differential phases from each waveguide, thus focusing to a tight spot at a displaced location due to the linear phase variation across the array, thereby leading to the spatial dispersion. Our

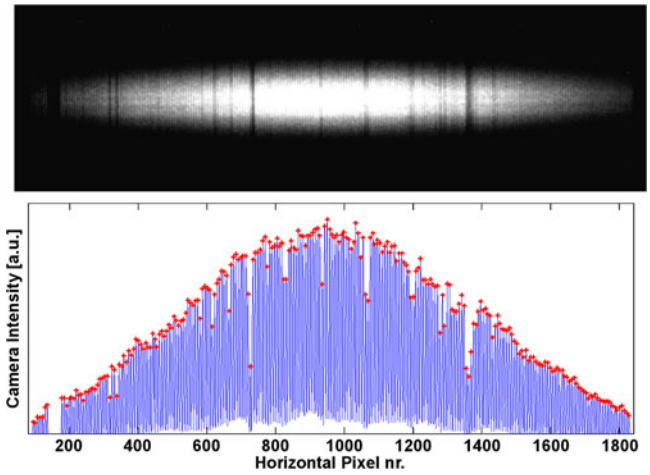

Fig. 4. Top: Direct image of light at the PLC output facet. Vertical axis is stretched due to cylindrical collimating lens. Bottom: Location of waveguides on SLM. A few waveguides have imperfections effecting light transmission through them.

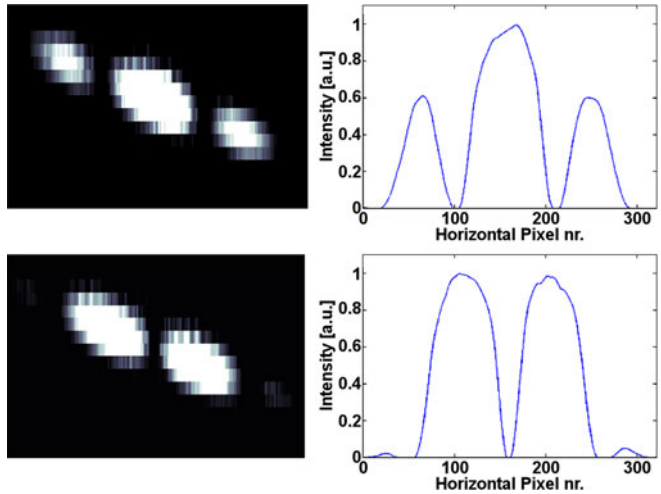

Fig. 5. Interference pattern of a waveguide pair of the imaged PLC observed at the Fourier plane camera, used to bring the waveguides into identical phase. Waveguide pair in phase (Top) and π out of phase (Bottom).

free-space solution currently supports one polarization state, but polarization diversity can be easily introduced to handle both polarization states which has not been attempted in this work.

Prior to setting the phase LCoS SLM to adjust the waveguide phases, we place an infrared (IR) camera at the image plane to directly observe the PLC output facet (Fig. 4-top). The image of the output waveguide array is obtained. The waveguide modes are vertically elongated due to the cylindrical collimation lens affixed to the PLC. The intensity of light across the array is Gaussian distributed, as expected through a slab lens excitation, with few waveguides exhibiting excess loss due to lithography imperfections. These amplitude variations, amounting to the a_i terms of Eq. 1, can modify the constructive mode shape at the Fourier plane. Since they are few their impact is minimal.

The procedure for establishing the amount of phase correction per waveguide in the array begins by first placing the LCoS SLM at the WGR image plane and moving the IR camera to the Fourier plane (in place of the spectral plane SLM seen in Fig. 3). The locations of the individual waveguides on the image plane SLM pixels were registered by writing a phase ramp pattern five pixels wide (to tilt the light falling on the SLM towards the pickup mirror and spectral plane) and scanning it across the SLM while registering the power reaching the camera, from which we deduce the waveguides center locations (Fig. 4-bottom). Next, we broaden the rectangle to capture two waveguides modes at a time (14 pixels wide), and examine the interference pattern in the Fourier plane for each successive waveguide pair. This is analogous to Young's double slit experiment; when the waveguides are in phase the interference pattern forms a dominant central lobe and weak side lobes on either side. When the two waveguides are out of phase (shifted by π), the interference pattern is that of two equal peaked lobes (with a null in the center). Images of these interference patterns collected by the camera are shown in Fig. 5.

By modifying the reflected phase of one waveguide from the pair while monitoring the far field interference, we can set the two waveguides to be in equal phase. This is done by adding a 7 pixel wide phase offset to one of the two interfering beams, in addition to the phase ramp for selecting the two beams. All the waveguides´ phases were set to reflect a constructive interference using this technique, and the phase correction terms collected. This procedure starts from the center (most intense) waveguide, and proceeds right to the array edge one waveguide at a time to set equal phase as the predecessor, and then correcting the left half starting from the center in the same manner. Greatest sensitivity was obtained by comparing the area beneath the two side peaks.

When encountering an inactive waveguide (no light emerging), the interference is collected between the waveguides before and after the inactive zone. This increases the spatial modulation frequency on the far field beam, but the symmetry criterion can still be identified, to maintain phase continuity across the gap.

The phase corrections that are required for each waveguide are thus completely known and can now be applied simultaneously on the LCoS SLM to correct the phase response of the entire WGR output. The correction values and the LCoS phase pattern are shown in Fig. 6.

These phase corrections appear quite random, spaced between 0 and 2π across the array (with possible multiples of 2π which we cannot distinguish). These phase errors are the explanation as to why the phased array did not function as planned, as they constitute a random phase realization as opposed to equal phase, and the far field pattern of a random phase distribution is spread out instead of focusing to a spot. One of the advantages of the phase correction with the LCoS SLM is that we can independently access each waveguide with one single device. Alternatively, one could place individual thermo-optic (TO) modulators on each waveguide to phase correct them one by one [20]. However, such TO modulators are power hungry, and can cause thermal crosstalk between adjacent waveguides. Similarly, the waveguide array could be implemented in electro-optic waveguide material, allowing electrical tuning [21]. Still electro-optic tuning typically operates over single polarization. Alternatively, the waveguides can be permanently trimmed with

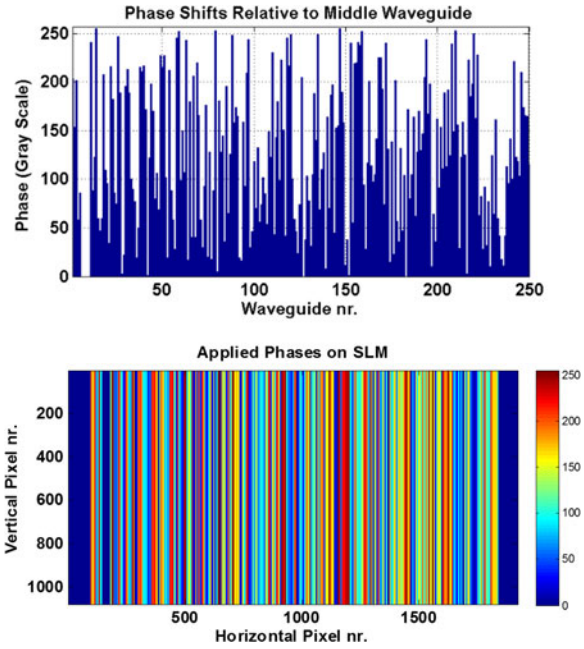

Fig. 6. Top: Waveguide phase errors relative to the centermost waveguide. Bottom: Phase shift pattern written to the SLM.

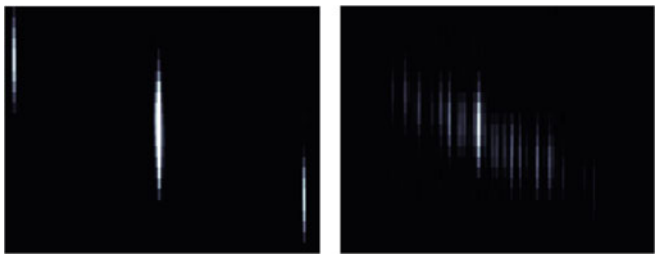

Fig. 7. Far field radiation patterns for CW excitation laser wavelength. Left: with applied phase correction. Right: without phase correction.

a UV laser [22], however this operation can be optimized for one polarization only. In the free-space solution we employed, it is possible to treat each polarization separately by introducing a polarization diversity solution in the form of a walkoff crystal and a half-wave plate, such that the output light is divided to two co-propagating beam arrays of the same polarization. The imaging arrangement would observe two sets of WGR outputs, one per polarization.

With the camera still mounted at the Fourier plane, we can now directly observe the far field radiation pattern of the entire array (as opposed to the pair-wise radiation pattern of Fig. 5). When phase corrections are applied, the far field pattern constructively focuses to a spot with the corresponding higher orders (Fig. 7-left). Tuning the center wavelength causes the focus spot position to shift, linearly with wavelength, in accordance with the spatial dispersion. If we turn off the LCoS phase compensation and directly image the cumulative far field radiation pattern (with the phase errors), we observe a random, speckle-like interference pattern spanning a wide field (Fig. 7-right), which still shifts in location with wavelength, but is not spectrally resolved.

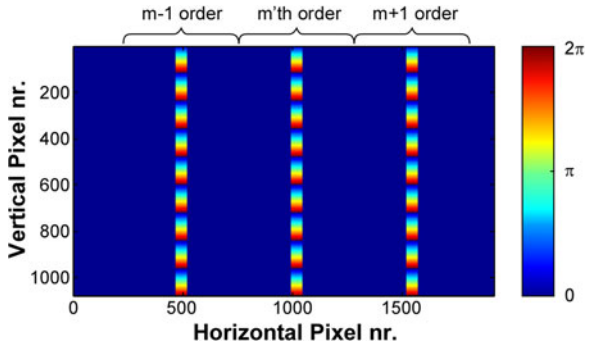

Fig. 8. Phase function written to the SLM, for selecting 20 GHz wide band, including light falling on adjacent diffraction orders for flat spectral responsivity across the WGR's 200 GHz wide FSR.

IV. Fine Resolution PSP Characterization

To complete the PSP construction, we replace the IR camera at the spectral plane with a second LCoS SLM to return all the light back to the first LCoS SLM and then to the WGR and output fiber. The SLM was placed at a slight tilt diverting all light out the optical path (to eliminate the cover glass back reflection). An attenuation lookup table was created to calibrate the linear phase ramp on the SLM for a selected coupling loss. The look up table was made by first locating the beams' vertical center on the SLM by a $0/\pi$ phase step scan, then proceeding to register the attenuation from different linear phase ramps (tilt angles). Since each spectral component excites few diffraction orders, we back reflect them all to collect all the energy. This is done by repeating the frequency selection pattern on the SLM with offsets corresponding to the diffraction orders (Fig. 8). The diffraction orders are spatially separated by $\lambda_0 \cdot f/p$ equaling 521 LCoS pixels (see Eq. (2)). Selecting a frequency band in this manner achieves uniform performance no matter where the frequency band occurs with respect to the WGR's 200 GHz wide FSR, and that indeed the response is periodic (Fig. 9-top).

The hallmark of our processor is its spectral resolution, hence it is important to define this metric and how it can be experimentally assessed. The dispersed optical signal is described by Eq. (2). Each spectral component is focused to a Gaussian spot size of $\Delta_{\mathrm{cw}} = 2w_0$ at a unique position (we now neglect the additional diffraction orders for brevity), and the spectra is linearly dispersed as set by $dx/d\nu$. We propose to define the spectral resolution as the ratio relating the beam radius to the spatial dispersion term, according to $\nu_{\mathrm{res}} = w_0/(dx/d\nu)$. We next prove this spectral resolution metric is sensible for assessing the performance of a PSP.

Let the LCoS select a spatial extent Δx about x_c (the position of center frequency ν_c). Performing the overlap integral over the spatial coordinate x, yields the coupling strength for every spectral component [6]:

$$|\eta(\nu)|^2 = \frac{1}{4}\left(\mathrm{erf}\left[\frac{\sqrt{2}}{w_0}\left(\frac{\Delta x}{2} + \frac{dx}{d\nu}(\nu-\nu_c)\right)\right] + \mathrm{erf}\left[\frac{\sqrt{2}}{w_0}\left(\frac{\Delta x}{2} - \frac{dx}{d\nu}(\nu-\nu_c)\right)\right]\right)^2 \quad (4)$$

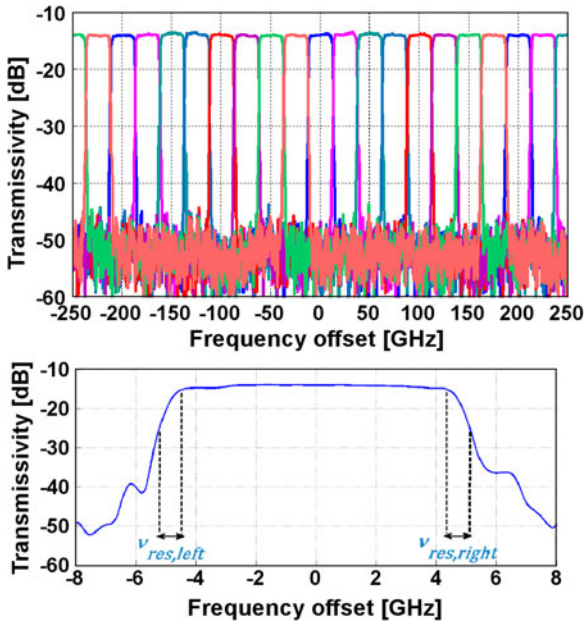

Fig. 9. Optical band selection. Top: Selection of 10 GHz wide bands anywhere within the 200 GHz FSR. Bottom: Resolution metrics of 0.8 GHz, measured from −0.5 dB (10%) down to −10 dB (90%).

where erf(•) is the error function. Substituting $\Delta x = (dx/d\nu) \cdot \Delta\nu$ and using our resolution definition for $\nu_{\rm res}$, we obtain

$$|\eta(\nu)|^2 = \frac{1}{4}\left(\operatorname{erf}\left[\frac{\sqrt{2}}{\nu_{\rm res}}\left(\frac{\Delta\nu}{2}+(\nu-\nu_c)\right)\right] + \operatorname{erf}\left[\frac{\sqrt{2}}{\nu_{\rm res}}\left(\frac{\Delta\nu}{2}-(\nu-\nu_c)\right)\right]\right)^2 \quad (5)$$

Each error function in Eq. (5) defines the spectral roll-off at the corresponding spectral edge. (Note that Eq. (5) slightly differs from the equation provided in Ref. [23] which uses a metric σ, due to differing definitions of our resolution metric, $\nu_{\rm res}$, which essentially equals 2σ but is directly measurable as demonstrated next.) Under the assumption that the two edges do not overlap (which occurs for sufficiently large bandwidth selection, $\Delta\nu$, relatively to $\nu_{\rm res}$), then each error function defines the edge roll-off independently. Many metrics may be used to assess the roll-off from the pass-band to the block-band. Using the 90%-10% transition (analogous to −0.5 dB to −10 dB transition), we evaluate the erf(•) values in Eq. (5) leading to the target measures, and find that the difference in the two arguments is 1.436. Hence the transition occurs over a bandwidth of $1.436 \cdot \nu_{\rm res}/\sqrt{2} \approx \nu_{\rm res}$. The 90-10 transition bandwidth is easy to identify and measure (Fig. 9-bottom) and is equivalent to directly measuring the dispering optics′ resolution. Likewise, we can also predict the transition from −0.5 dB down to −20 dB ($1.4 \cdot \nu_{\rm res}$) and down to −30 dB ($1.667 \cdot \nu_{\rm res}$). If we wish to maintain −40 dB isolation between adjacent channel components we can adopt a $1.9 \cdot \nu_{\rm res}$ metric for WDM signal separation, which can be rounded to $2 \cdot \nu_{\rm res}$ for the transition bandwidth between two separate channels (with a safety margin).

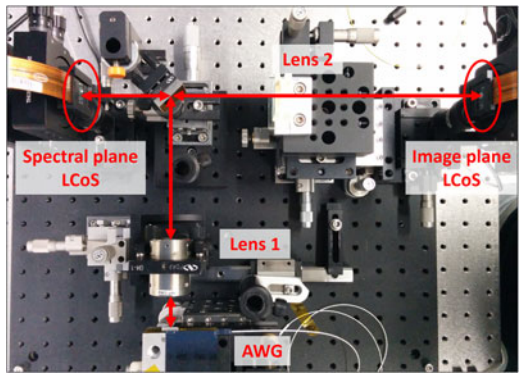

Fig. 10. Photo of the experimental setup for compensation of WGR phase errors with an LCoS phase modulator and spectral processing in the Fourier plane.

In addition to the resolution metric, a PSP is also characterized by the positional accuracy at which it is possible to encode a spectral function on the LCoS SLM. This positional accuracy is defined by the spectral addressability. Knowing the spatial dispersion term and LCoS pixel size, the spectral addressability is (*LCoS pixel size*)/$(dx/d\nu)$. In our PSP implementation the LCoS pixel size is 8μm and the spatial dispersion equals 20 μm/GHz, yielding 400 MHz addressability for our PSP.

All our PSP characterization was performed with a swept laser interferometry technique (using a Luna Technologies optical vector analyzer), as instruments such as grating based optical spectrum analyzers do not offer sufficient spectral resolution. The 0.8 GHz spectral resolution was confirmed by measuring the 90-10 transition bandwidth, which is in line with the resolution definition $\nu_{\rm res} = w_0/(dx/d\nu)$, where $\Delta_{\rm cw} = 2w_0 = 32\,\mu$m.

The focused spectral spot shows some deviation from a smooth Gaussian characteristic (defined by Eq. (5)) as witnessed by a lobe in the transition band occurring about −20 dB down (Fig. 9-bottom). This may be due to imperfect phase compensation or the amplitude deviations from Gaussian apodization. The pixel to frequency mapping shows that a 400 MHz addressability was obtained.

With this current setup (Fig. 10) the measured loss is −14 dB. The identified loss mechanisms are as follows: WGR fiber coupling efficiency (×2) −6 dB, LCoS SLM (×3 reflections) −4 dB and optical circulator (×2) −2 dB. The total known loss amounts to −12 dB, leaving unaccounted losses of 2 dB that are likely from inefficiency of optical collimation and focusing back to WGR. While this loss is high, it can be improved by employing two WGR (eliminating the circulator) [24], and with WGR techniques not involving the LCoS SLM [22], to a ∼−6 dB level. We also observe that our dispersed spectra is slanted in all our images (Figs. 5 and 7). This is most likely due to a small roll angle between the attached cylindrical lens and the PLC, which probably accounts for some of the unaccounted losses.

V. Processing Optical Communication Signals

To demonstrate the capabilities of the fine resolution processor, we performed various tests using synthesized optical

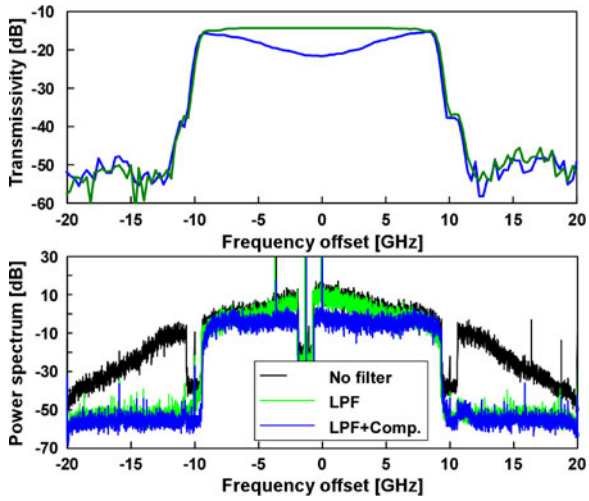

Fig. 11. Shaping of a 20 GHz DFT-S OFDM channel with DAC response compensation. Top: The calculated optical response of the PSP. Bottom: Detected spectra without and with optical filters with the respective compensation.

communication signals with digitally-fed D/A converters driving a nested IQ-modulator (single polarization), and processed the optical signal with the fine resolution processor for applications such as transmitter-side all-optical Nyquist shaping, and OFDM subcarrier selection out of a wideband superchannel. The received optical signals were pre-processed by an optical modulation analyzer (OMA) and the optical responses of the PSP were captured with an optical vector analyzer.

We first demonstrate the PSP ability to optically filter out DAC harmonic images and compensate for its inhomogeneous frequency response, by placing our PSP at the transmitter end, in order to shape a 20 GHz wide optical multi-sub-band channel featuring 16 sub-bands. The signal was digitally synthesized, based on the recent filter-bank based sub-band DSP paradigm [26]. Each 1.25 GHz-wide sub-band contained an effective Nyquist-shaped carrier, digitally generated by DFT-spread OFDM [27] with 64 subcarriers per sub-band, each 16-QAM modulated (thus 1024 OFDM subcarriers over the full channel, carrying an aggregate rate of 80 Gb/s over a single polarization).

One of the 16 sub-bands (located mid-band) was dedicated to carrying a lone pilot tone, for frequency offset compensation and linear and nonlinear phase recovery at the receiver [28]. The PSP was used to filter out the baseband DAC image (20 GHz wide) as well as equalize the frequency response throughout the signal by applying the inverse DAC frequency response (see Fig. 11). The generated signal exhibited improved BER, as measured by the OMA, for long haul systems.

We next set the PSP for transmitter shaping of Nyquist WDM signals, realizing raised-cosine optical filters with various roll-off factors (see Fig. 12). The 20 GHz wide filters were used to shape the output optical signal from the modulator when fed by a 20 Gbaud, 16-QAM data stream (one sample per symbol). The signal was again analyzed with an OMA, which performed the digital signal processing (DSP) and estimated the error vector magnitude (EVM), with minor performance degradation even as the roll-off factors decreased and the filter exhibited sharper, more rectangular edges. The filter optical impulse response was

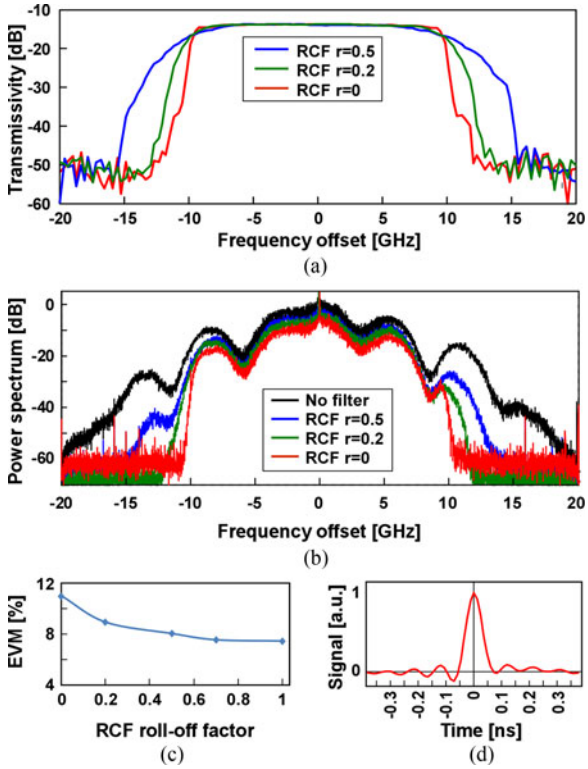

Fig. 12. Nyquist-shaping via optical filtering for 20 Gbaud QAM-16 generation. (a) 20 GHz wide raised-cosine shaping filters. (b) Detected power spectrum with and without shaping filters. (c) Coherent receiver EVM as function of raised cosine roll-off factor. (d) Filter's finite impulse response.

measured by transmitting a symbol corresponding to single bit embedded in multiple null symbols, and coherently detecting the lone symbol response; after spectral shaping, the resulting temporal response for the 20 GHz-wide rectangular filter shape appeared sinc-like, even as the filter was narrowed down to 4 GHz. At very narrow filter settings, the finite fine resolution resulted in temporal pulses with no sidelobes, demonstrating that the shaping filter is capable of sharp narrowband Nyquist shaping down to several GHz.

We next demonstrated matched optical filtering for OFDM subchannel extraction from a multi-carrier superchannel having overlapping spectral extent. We synthesized a 20 GHz wide superchannel having multi-carrier OFDM signal. QPSK OFDM subchannels were digitally synthesized with 5, 8 or 12 subcarriers at 4, 2.5 and 1.5 GHz respective spectral spacings, forming a rectangular power spectrum. We then placed our PSP ahead of a coherent receiver for selective extraction of individual OFDM subcarriers out of a 20 GHz full channel (Fig. 13). The photonic processor was programmed for sinc-shaped matched optical filtering to a chosen subcarrier, by scaling the sinc shape to the baud rate and placing it a spectral offset tuned to the particular selected OFDM subcarrier. The spectral filter is encoded by the phase LCoS SLM in amplitude by angle detuning the reflected beam and with positive/negative phases of the sinc lobes with 0, π phase jumps. Following the optical matched filtering, the signal is detected by a "slow" QPSK single-carrier coherent receiver, which samples in time at the open eye position and

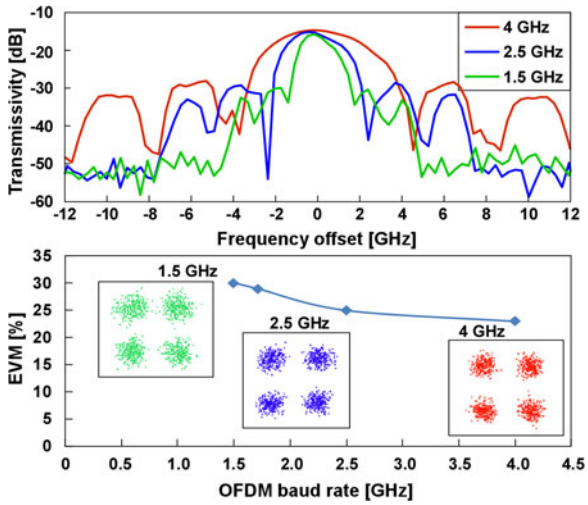

Fig. 13. OFDM optical demultiplexing. Top: Sinc-shaped optical filters as narrow as 1.5 GHz. Bottom: Measured receiver performance of optically demultiplexed signals. As the baud rate becomes smaller, the sinc-shaped filter quality deteriorates gradually, as witnessed by the EVM.

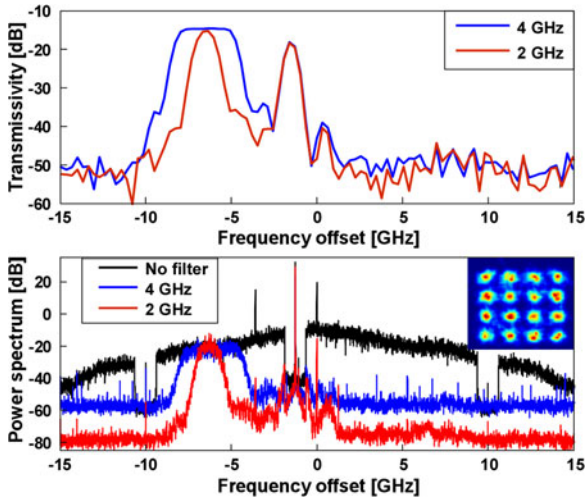

Fig. 14. DFT-S OFDM drop-demux cherry picks sub-band + distant pilot tone. Top: Narrow bandwidth optical filters extract single 1.25 GHz sub-band plus a pilot tone 5 sub-bands away. Bottom: Detected spectra without and with optical filters with respective 4, and 2 GHz bandwidth. (Inset) Received 16- QAM constellation.

measures the EVM metric [25]. The dominant identified impairment was the laser phase noise, enhanced by the very low baud rates (walkoff over long duration symbols).

A final example demonstrated sub-band add/drop capabilities of our PSP for the same signal used to demonstrate spectral flattening (with 20 GHz wide spectrum consisting of 16 Nyquist shaped sub-bands, each 1.25 GHz wide, carrying 16-QAM single polarization modulation). In order to establish an initial baseline, we coherently demodulated the full 20 GHz channel and performed in DSP filter-bank based sub-band decomposition and DFT-despreading as per [26], with one extension: The lone pilot in the mid sub-band extracted by a digital filter in the filter-bank arm, and the filtered pilot was used to demodulate all the other sub-bands. Finally, we demonstrated a novel drop-demultiplexing capability, extracting at-will any one of the 1.25 GHz wide sub-bands out of the 20 GHz channel spectrum while filtering away the remaining sub-bands, with the exception of the sub-band containing the lone-pilot-, which was also photonically extracted (see the two peaks in Fig. 14-Top). Using the lone pilot in the DSP domain to robustly demodulate the dropped sub-band, resulted in nearly perfect cancellation of the laser phase noise and frequency offset out of the dropped sub-band, as the phase-noise/frequency-offset impairments are common to both the sub-band data and the lone pilot hence their subtraction upon demodulation yielded nearly null residual phase noise. This demonstrated a robust detection method for the 1.25 GHz dropped sub-band. The 5 Gb/s sub-band signal quality was measured to have been just slightly decreased upon propagation via the dropping filter; EVM increasing gradually from 16.2% at broadband to 20.1% at 2 GHz width.

VI. Conclusion

We introduced a fine resolution spectral processor based on a WGR dispersive element having 200 GHz FSR with a phase SLM used for imparting arbitrary amplitude and phase transfer functions. To achieve fine resolution, the WGR incorporates long waveguides that are susceptible to phase errors. Those fabrication phase errors were corrected with an active LCoS phase SLM in the image plane of the WGR output. By properly correcting the phase errors we obtain the WGR's spectral resolving power. This allowed performing spectral manipulation with 0.8 GHz resolution and 400 MHz addressability within a 200 GHz FSR. The novel PSP capabilities were demonstrated in a several data-transmission contexts, such as spectral shaping, sub-band demux and matched filtering with nearly ideal characteristics. Such capabilities are required to support 1 Tb/s superchannel transmission with subcarrier optical add/drop capabilities.

Acknowledgment

The authors acknowledge the assistance of C. R. Doerr in the design of the WGR.

References

[1] M. A. F. Roelens *et al.*, "Dispersion trimming in a reconfigurable wavelength selective switch," *J. Lightw. Technol.*, vol. 26, no. 1, pp. 73–78, Jan. 2008.

[2] R. Schmogrow *et al.*, "Pulse-shaping with digital, electrical, and optical filters-A comparison," *J. Lightw. Technol.*, vol. 31, no. 15, pp. 2570–2577, Aug. 2013.

[3] H. Hu, D. Kong, E. Palushani, M. Galili, H. C. H. Mulvad, and L. K. Oxenløwe, "320 Gb/s Nyquist OTDM received by polarization-insensitive time-domain OFT," *Opt. Express*, vol. 22, pp. 110–118, 2014.

[4] C. Froehly, B. Colombeau, and M. Vampouille, "Shaping and analysis of picosecond light pulses," *Progress Opt.*, vol. 20, pp. 63–153, 1983.

[5] A. M. Weiner, "Femtosecond pulse shaping using spatial light modulators," *Rev. Sci. Instrum.*, vol. 71, pp. 1929–1960, 2000.

[6] D. M. Marom *et al.*, "Wavelength-selective 1 × K switches using free-space optics and MEMS Micromirrors: Theory, design, and implementation," *J. Lightw. Technol.*, vol. 23, no. 4, pp. 1620–1630, Apr. 2005.

[7] S. Frisken, S. B. Poole, and G. W. Baxter, "Wavelength-selective reconfiguration in transparent agile optical networks," *Proc. IEEE*, vol. 100, no. 5, pp. 1056–1064, May 2012.

[8] C. Xie, L. Möller, and R. Ryf, "Improvement of optical NRZ- and RZ-duobinary transmission systems with narrow bandwidth optical filters," *IEEE Photon. Technol. Lett.*, vol. 16, no. 9, pp. 2162–2164, Sep. 2004.
[9] D. Sinefeld and D. M. Marom, "Hybrid guided-wave/free-space optics photonic spectral processor based on LCoS phase only modulator," *IEEE Photon. Technol. Lett.*, vol. 22, no. 7, pp. 510–512, Apr. 2010.
[10] D. Sinefeld, S. Ben-Ezra, and D. M. Marom, "Nyquist-WDM filter shaping with a high-resolution colorless photonic spectral processor," *Opt. Lett.*, vol. 38, pp. 3268–3271, 2013.
[11] M. Shirasaki, "Chromatic dispersion compensator using virtually imaged phased array," *IEEE Photon. Technol. Lett.*, vol. PLT-9, no. 12, pp. 1598–1600, Dec. 1997.
[12] G. H. Lee, S. Xiao, and A. M. Weiner, "Optical dispersion compensator with >4000-ps/nm tuning range using a virtually imaged phased array (VIPA) and spatial light modulator (SLM)," *IEEE Photon. Technol. Lett.*, vol. 18, no. 17, pp. 1819–1821, Sep. 2006.
[13] K. Takada, M. Abe, T. Shibata, and K. Okamoto, "1-GHz-Spaced 16-channel arrayed-waveguide grating for a wavelength reference standard in DWDM network systems," *J. Lightw. Technol.*, vol. 20, no. 5, pp. 850–853, May 2002.
[14] R. Rudnick, D. Sinefeld, O. Golani, and D. Marom, "One GHz resolution arrayed waveguide grating filter with LCoS phase compensation," in *Proc. Opt. Fiber Commun. Conf.*, 2014, Paper Th3F.7.
[15] R. Rudnick *et al.*, "Sub-banded/single-sub-carrier drop-demux and flexible spectral shaping with a fine resolution photonic processor," in *Proc. Eur. Conf. Opt. Commun.*, 2014, Paper PD4.1.
[16] C. Dragone, "An N∗N optical multiplexer using a planar arrangement of two star couplers," *IEEE Photon. Technol. Lett.*, vol. PLT-3, no. 9, pp. 812–815, Sep. 1991.
[17] K. Okamoto, K. Takiguchi, and Y. Ohmori, "16-channel optical add/drop multiplexer using silica-based arrayed-waveguide gratings," *Electron. Lett.*, vol. 31, pp. 723–724, 1995.
[18] L. H. Spiekman *et al.*, "Design and realization of polarization independent phased array wavelength demultiplexers using different array orders for TE and TM," *J. Lightw. Technol.*, vol. LT-14, no. 6, pp. 991–995, Jun. 1996.
[19] D. Klonidis *et al.*, "Enabling transparent technologies for the development of highly granular flexible optical cross-connects," in *Proc. 16th Int. Conf. Transp. Opt. Netw.*, 2014, pp. 1–6.
[20] J. Doylend, M. R. Heck, J. Bovington, J. Peters, L. Coldren, and J. Bowers, "Free-space beam steering in two dimensions using a silicon optical phased array," in *Proc. Opt. Fiber Commun. Conf.*, 2012, Paper OM2J.1.
[21] T. McDermott and T. Brewer, "Large scale IP router using a high speed optical switch element," *J. Opt. Netw.*, vol. 2, pp. 229–240, 2003.
[22] N. Goldshtein *et al.*, "Fine resolution photonic spectral processor using a waveguide grating router with permanent phase trimming," *J. Lightw. Technol.*, vol. 34, no. 2, pp. 379–385, Jan. 2016.
[23] C. Pulikkaseril, L. A. Stewart, M. A. F. Roelens, G. W. Baxter, S. Poole, and S. Frisken, "Spectral modeling of channel band shapes in wavelength selective switches," *Opt. Express*, vol. 19, pp. 8458–8470, 2011.
[24] D. M. Marom, C. R. Doerr, M. Cappuzzo, E. Chen, A. Wong-Foy, and L. Gomez, "Hybrid free-space and planar lightwave circuit wavelength-selective 1 × 3 switch with integrated drop-side demultiplexer," in *Proc. Euro. Conf. Opt. Commun.*, 2005, pp. 993–994.
[25] D. Hillerkuss *et al.*, "Simple all-optical FFT scheme enabling Tbit/s real-time signal processing," *Opt. Express*, vol. 18, pp. 9324–9340, 2010.
[26] M. Nazarathy and A. Tolmachev, "Subbanded DSP architectures based on underdecimated filter banks for coherent OFDM receivers: Overview and recent advances," *IEEE Signal Process. Mag.*, vol. 31, no. 2, pp. 70–81, Mar. 2014.
[27] T. Yan, W. Shieh, and B. S. Krongold, "DFT-spread OFDM for fiber nonlinearity mitigation," *IEEE Photon. Technol. Lett.*, vol. 22, no. 16, pp. 1250–1252, Aug. 2010.
[28] L. B. Du and A. Lowery, "Experimental demonstration of pilot-based XPM nonlinearity compensator for CO-OFDM systems," in *Proc. Eur. Conf. Opt. Commun.*, 2011, Paper Th.11.B.4.

Authors' biographies not available at the time of publication.